Supplementary Information

Ultra-thin lamellar material-based sensors for low-cost, ultrasensitive quantification of serum neurofilament light chain for neurological diagnosis

Mosarof Hossain[1], Dhamidhu Eratne[2,3], Marian Todaro[1], Ben Rollo[1], Neha Kaul[1], Dennis Velakoulis[2], Terence J. O'Brien[1], Patrick Kwan[1]**

1. Department of Neuroscience, School of Translational Medicine, Faculty of Medicine, Nursing and Health Sciences, Monash University, Melbourne, Victoria, 3004, Australia.
2. Neuropsychiatry Centre, The Royal Melbourne Hospital, Melbourne, VIC, Australia
3. Department of Psychiatry, University of Melbourne, Melbourne, VIC, Australia

Table of Contents

S1 - Materials synthesis and Sensor fabrication

Fig. S1 illustrates the wafer-scale fabrication process of the LM-FET sensors. Briefly, p-type Si wafers were purchased from MCN and sequentially cleaned with acetone and isopropyl alcohol (IPA) in an ultrasonic bath, followed by piranha ($H_2SO_4 : H_2O_2$) treatment to remove organic residues and improve surface hydrophilicity. A ~285 nm SiO_2 layer was then deposited on the Si substrate via e-beam evaporation to serve as the gate dielectric of the LM-FET sensor. Using standard photolithography method, we fabricated three Cr-coated glass masks (materials, electrode and oxide layer) using maskless aligner (Heidelberg MLA150). A positive photoresist (AZ1512 HS) was spin-coated onto the Si/SiO_2 wafers and soft-baked at 110 °C for 90 s. The coated wafers were aligned with the mask and exposed to UV light using the mask aligner (SUSS MA6), followed by development with AZ 726 developer (~60 s) to define the patterned regions. Subsequently, ultra-thin multilayer films (~40 nm total thickness) were deposited by e-beam evaporation at a controlled rate (~0.1 Å/s). The lamellar structure consisted of sequential deposition of TiO_2 (15 nm), Si (5 nm), TiO_2 (15 nm) and Pt (5 nm), forming a ultra-thin film based conductive multilayer channel. Lift-off was performed by immersing the wafers in acetone, followed by IPA rinsing and N_2 drying to remove unwanted material. Post-deposition annealing was carried out at 400 °C for 1 h under Ar flow (200 sccm) using the MTI furnace to improve film uniformity, interfacial adhesion, and electrical properties. This annealing process enabled the deposited ultra-thin multilayered materials to transform into ultra-thin lamellar materials. For LM-FET sensor development, Ti/Au (7/100 nm) source and drain electrodes and an Al_2O_3 passivation layer of 70 nm were defined using photolithography, e-beam deposition, and lift-off process [1, 2]. The wafers were then protected with a photoresist layer for storage and subsequently diced into ~60 individual chips using a dicing saw (DAD 3350). Prior to use, the protective layer of the LM-FET sensor was removed and cleaned with acetone and IPA using ultrasonic bath. A final annealing step at 180 °C for 1 h under forming gas (H_2/Ar: 10/100 sccm) was performed to reduce contact resistance of the metal electrodes and improve signal-to-noise ratio. This wafer-scale process enables reproducible fabrication of high-quality LM-

FET sensors with ultra-thin lamellar materials, suitable for reliable electrical characterisation and biosensing applications.

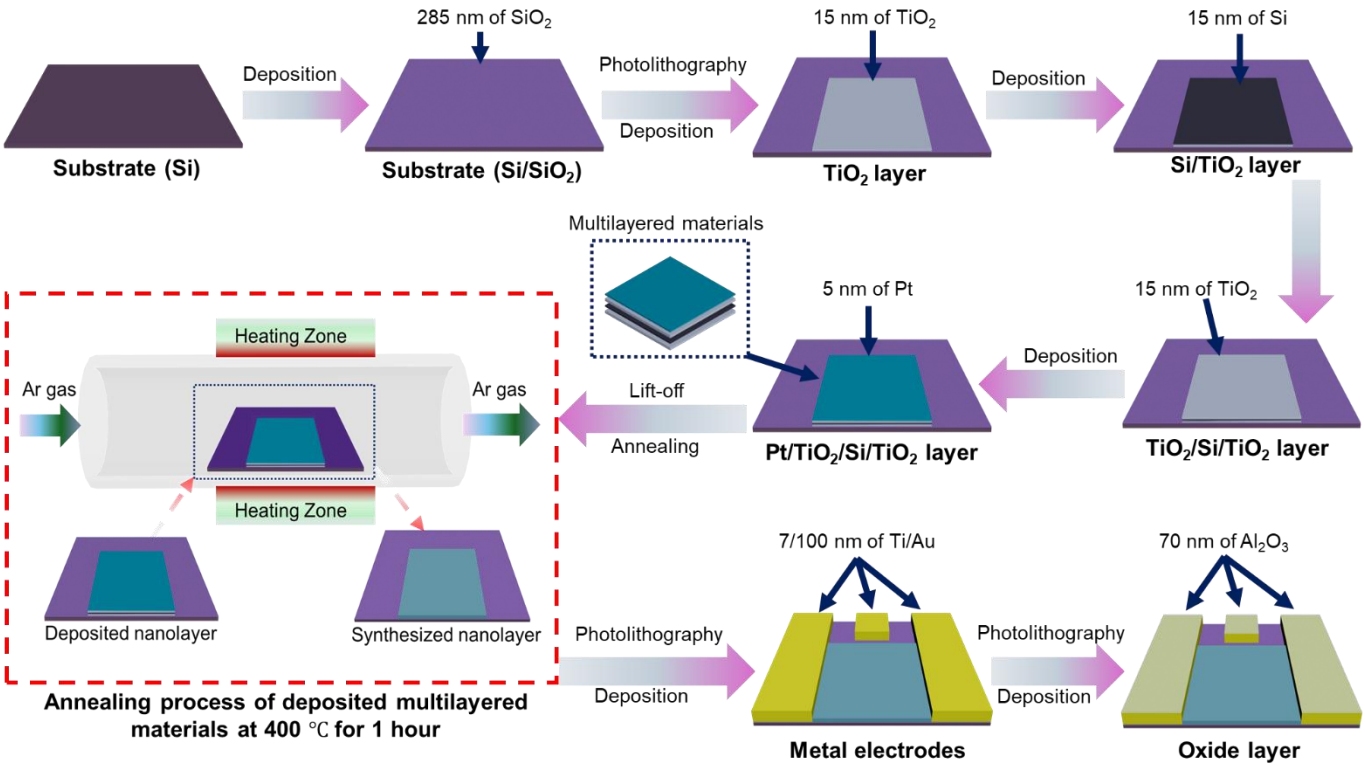

Fig. S1: *The ultra-thin lamellar materials synthesize process and LM-FET sensor fabrication process.*

a.

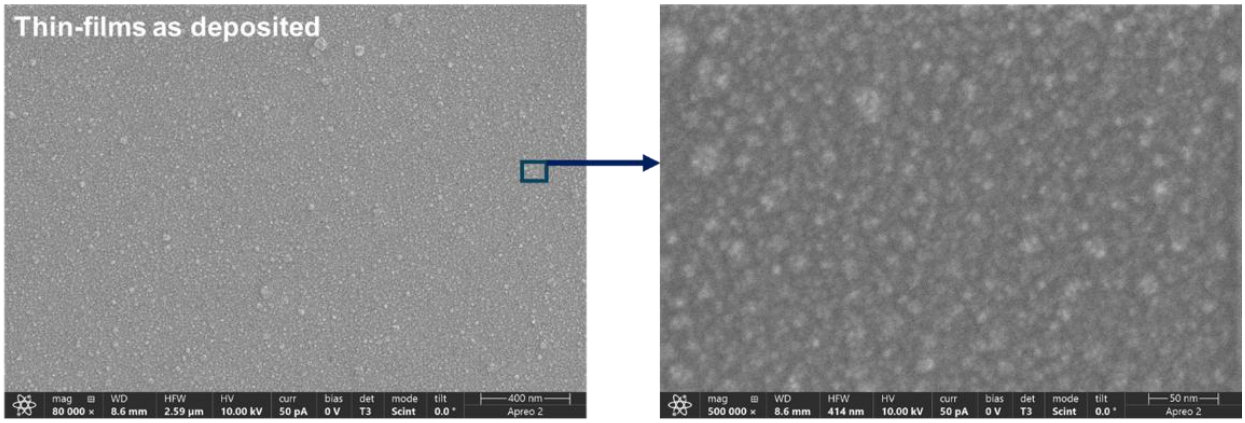

b.

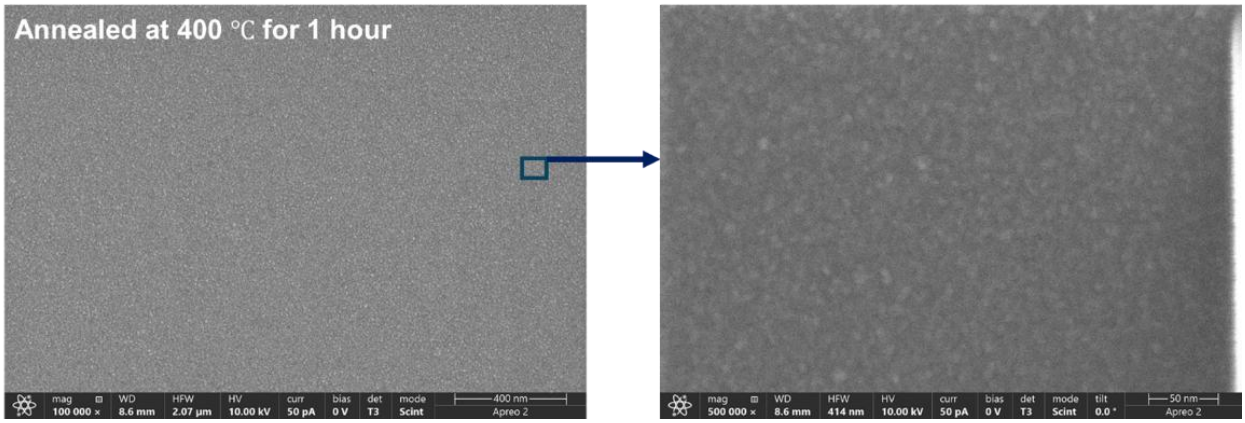

Fig. S2: *FEG-SEM images for the surface morphology of the ultra-thin lamellar materials (a) the deposited ultra-thin film based multilayered materials and (b) after annealing at* 400 ℃ *for 1 hour the multilayered formed a smooth and ultra-thin lamellar material.*

S2: EDX elemental analysis

Table S1 shows the elemental analysis of the ultra-thin film based lamellar materials before and after annealing. The quantitative EDX analysis further supports this transformation, showing an increase in Ti and Pt content (from ~0.1 to 0.4 at% and ~0.1 to 0.3 at%, respectively), while Si remains dominant due to the underlying substrate and O shows only minor variation. The relative increase in metal components after annealing reflects improved film continuity and reduced segregation, which are critical for establishing efficient charge transport pathways. Such compositional stabilization is known to reduce defect density and trap states, thereby enhancing carrier mobility and electrical performance of the LM-FET sensor [3, 4]. These structural and compositional improvements are consistent with the observed enhancement in LM-FET sensor performance after annealing, where the formation of a compact ultra-thin lamellar structure promotes stronger electrostatic coupling and more efficient modulation of sensing surface conductance. These results could be attributed by the thermal annealing in metal oxide–based ultra-thin films improves crystallinity, reduces interfacial disorder, and enhances electronic transport properties, which are essential for high-sensitivity biosensing applications [5, 6].

***Table S1*:** Quantitative comparison of atomic (%) and weight (%) compositions before and after annealing, obtained from EDX analysis.

Element	**Thin film as deposited**		**Annealed at 400 ℃ for 1 hour**	
	Atomic (%)	**Weight (%)**	**Atomic (%)**	**Weight (%)**
C	4.4	2.1	5.1	2.5
O	24.2	15.7	23.0	14.7
Si	71.2	81.2	71.2	80.0
Ti	0.1	0.3	0.4	0.7
Pt	0.1	0.7	0.3	2.1

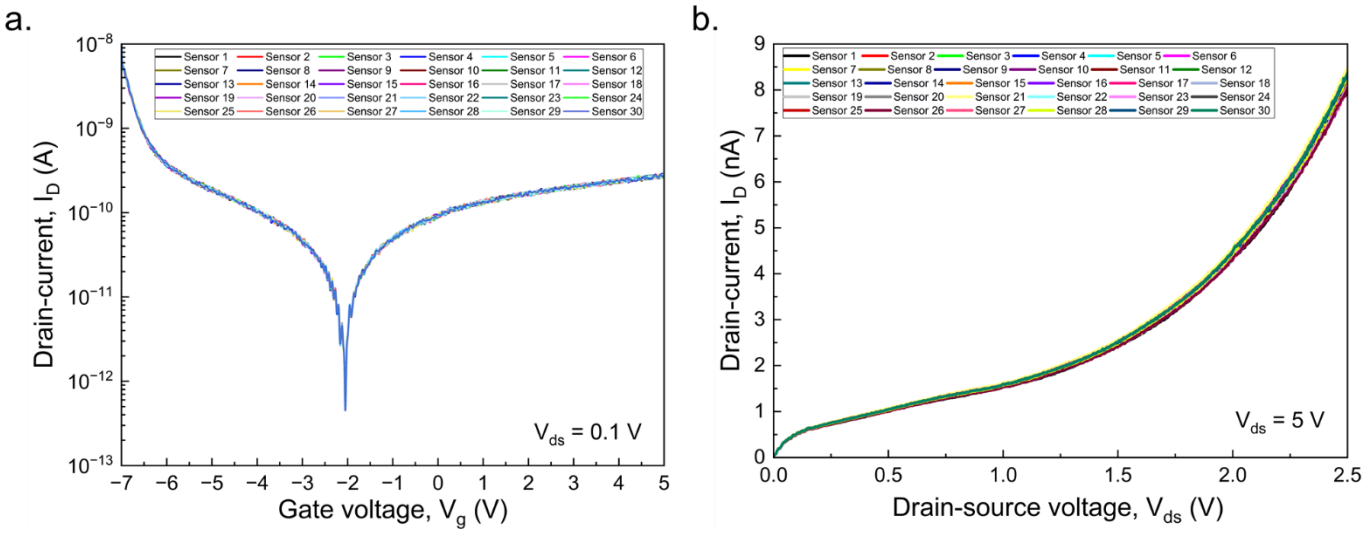

Fig. S3: *Reproducibility of the LM-FET sensors (n = 30). (a) Transfer characteristics measured over a gate voltage range of* -7 *to* $5\ V$ *at a constant drain–source voltage of* $0.1\ V$ *and (b) Output characteristics recorded by sweeping the drain–source voltage from* 0 *to* $2.5\ V$ *at a fixed gate voltage of 5 V, demonstrating consistent performance across the multiple LM-FET sensors.*

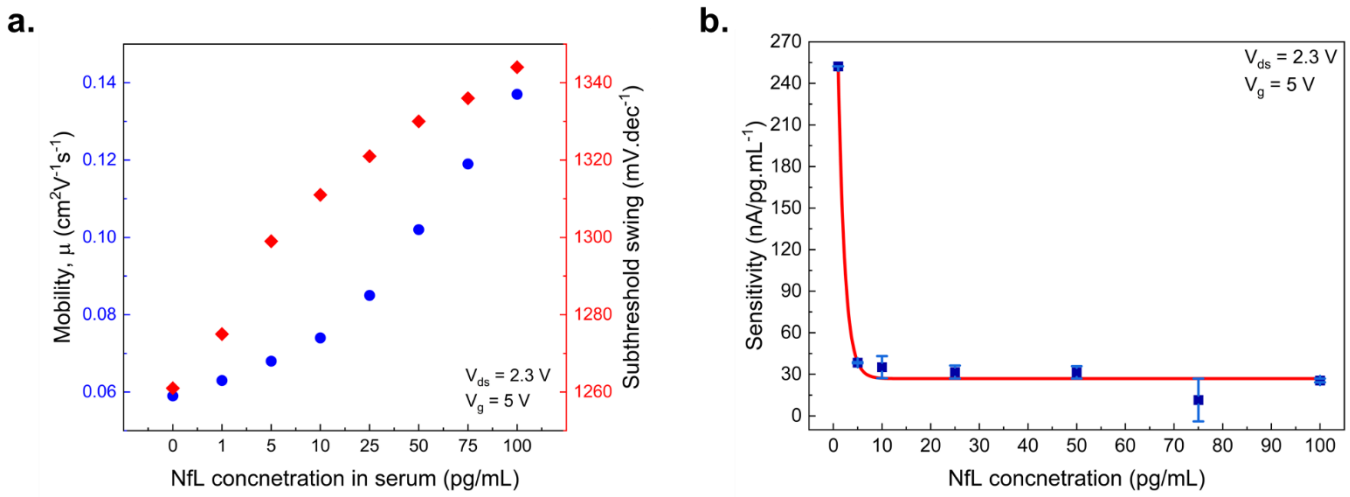

Fig. S4: *(a) The carrier mobility and subthreshold swing variation of the developed LM-FET sensor as a function of NfL concentration in serum. Extracted carrier mobility (μ, blue circles, left axis) and subthreshold swing (SS, red diamonds, right axis) of the LM-FET sensor as a function of NfL concentration (0–100 pg/mL) measured under fixed bias conditions at* $V_{ds} = 2.3\ V$, *and* $V_g = 5\ V$ *and (b) representing the sensitivity variation of the LM-FET sensor in the concentration range 1-100 pg/mL*

S3: Determination of Limit of detection (LOD) and limit of quantification (LOQ)

The analytical performance of the LM-FET sensor was assessed by determining the LOQ and LOQ using the IUPAC recommended signal-to-noise approach [7, 8]. The calibration curve (**Fig. 3e and 3f**) was constructed by plotting the normalized sensor response ($\frac{\Delta I_d}{I_0}$) as a function of NfL concentration and fitted using a linear regression model of $y = B + S.x$. Each concentration was measured in multiple replicates ($n = 12$), and the average response with corresponding standard deviation was used for fitting. The standard deviation of the blank signal (σ) was obtained from repeated measurements ($n = 12$) of serum without NfL, ensuring that the baseline noise reflects the real sensing environment. Prior to analysis, baseline correction was applied to account for sensor-to-sensor variation, and the response was normalised to the initial current (I_0) to minimise systematic deviations. The LOD and LOQ were determined using the 3σ and 10σ criteria, respectively, by the following equations

$$LOD = \frac{(I_{blank} - 3\sigma_{blank}) - B}{S}$$

$$LOQ = \frac{(I_{blank} - 10\sigma_{blank}) - B}{S}$$

where σ is the standard deviation of the blank signal, and S and B represent the slope and intercept of the calibration curve, respectively. The LOD defines the lowest concentration that can be reliably distinguished from background noise, while the LOQ corresponds to the minimum concentration that can be quantified with acceptable accuracy and precision.

Table S2: The analytical parameters and calculated LOD and LOQ for the LM-FET sensor.

I_{blank}	σ	S	B	LOD (pg/mL)	LOQ (pg/mL)
2.36E-08 (A)	7.74E-11 (A)	3.05E-08	2.31E-08	0.0076	0.025

Table S3: Performance comparison of the developed LM-FET sensor with reported technologies for NfL detection.

Detection method or Technology	**Sensing materials**	**Dynamic ranges (pg/mL)**	**Limit of detection (pg/mL)**	**Sample type**	**Sample Volume**	**Ref.**
Quanterix Simoa® NfL assay	NR	0-1800 (serum/EDTA plasma); 0 – 45,000 (CSF)	0.062	Human plasma, serum, and CSF	100 μL	[9, 10]
Simoa and Ella	Assay method	NR	0.0552	Plasma	NR	[11]
Micro drop electrochemical immuno biosensor	Gold electrode	NR	0.13 (PBS) 0.11 (Serum)	PBS and serum	20 μL	[12]
Portable electrochemical detector	Carbon surface	5.22–1000	5.22 pg/mL	Serum	50 μL	[13]
Electrochemical impedance immunoassay	Reduced graphene oxide screen-printed electrode	10 – 1,500	87 (serum) 390 (PBS)	PBS and Human serum	150 μL	[14]
Electrochemical immunosensor	Novel MOFs-derived material (ZrO2@La2O3)	50 – 200,000	12	PBS	NR	[15]
Photoelectrochemical detection	Pt nanowire arrays	0.1 – 1,000	0.0382	PBS and Plasma	60 μL	[16]
Extended gate in a field-effect transistor	Silicon nanowires coated with indium tin oxide	60 – 6×104 NDE/mL	60 – 6×104 NDE/mL	PBS and Plasma	200 μL	[17]
Graphene FET	Graphene	0.001– 10	0.57	Plasma	10 μL	[18]
Electrolyte-gated organic FET	Au substrate	100 fM – 100 nM	1.8	PBS	NR	[19]
Graphene-based FET sensor with integrated microfluidic device	Dual-channel graphene	0.1 – 1,000	55.63	PBS	20 $\mu L/min$	[20]
Nanotube-embedded organic electrochemical transistors immunosensor	Poly(EDOT–COOH–co-EDOT-EG3)	0.001 – 10,000	0.03277	PBS	NR	[7]
LM-FET sensor	**Novel ultra-thin lamellar materials**	**1 pg/mL – 100 pg/mL**	**0.0076**	**Human serum**	**3.0 μL**	**This work**

CSF: cerebrospinal fluids; MOFs:Metal organic frameworks; NDE: Neuron-derived Exosomes; NR: not reported

S4: Determination the concentration of NfL levels in serum

The current response of LM-FET sensor with clinical serum samples were evaluated and quantified using linear regression method. We have tested each collected serum sample in 6 replicates (n= 6) and recorded sensor response for the quantification of the NfL levels. We used previously established calibration curve from Fig. 3e, S4b and 3f and section S3 against the NfL concentration. The defined linear equation was directly used to calculate the NfL concentration in serum sample.

$$I_d = S.X + B$$

Where S is the slope of the calibration curve and B is the intercept. Rearrangement of this equation allowed direct conversion of the measured drain-current of LM-FET sensor into NfL concentration

$$X = \frac{I_d - B}{S}$$

Based on this linear regression equation, the drain-current of LM-FET sensor against clinical serum sample converted into NfL concentration using by following equation

$$X = \frac{\left(I_{d,clinical\ sample} - I_{Blank}\right) - B}{S}$$

Where $I_{d,clinical\ sample}$ is the drain current of LM-FET sensor with collected clinical sample, I_{Blank} is the mean drain-current of the LM-FET sensor with blank serum sample (Table S2). X is the calculated NfL concentration in pg/mL. We have calculated individual concentrations from each replicate using the above equation, and the final reported concentration was expressed as the mean ± standard deviation of the replicate-derived values. The coefficient of variation (CV, %) was also calculated to assess the reproducibility of the quantitative measurement (Table S5).

Table S4: Demographic details of the clinical samples tested. All patients had drug-resistant epilepsy.

Sample ID	Date of collection	Sex	Age at collection (years)
ANB035	13/03/2020	Male	91
ANB053	13/08/2020	Male	33
ANB077	14/10/2020	Female	35
ANB088	12/10/2021	Male	28
ANB092	20/01/2021	Female	48
ANB102	21/12/2020	Female	82
ANB107	19/01/2021	Female	25
ANB118	4/11/2021	Female	31
ANB148	3/06/2021	Female	28
ANB165	28/07/2021	Male	22
ANB233	16/03/2022	Female	70
ANB239	30/03/2022	Male	31
ANB261	5/05/2022	Male	21
ANB262	9/05/2022	Female	78
ANB263	9/05/2022	Female	56

Table S5: Calculated NfL concentrations in clinical serum samples for evaluating the quantitative performance of the LM-FET sensor

Sample ID	Mean (I_d)	I_d (serum)	Slope (S)	Intercept (B)	Concentration (pg/mL)
ANB035	1.20E-06	2.36E-08	3.05E-08	2.31E-08	37.74
ANB053	1.10E-06	2.36E-08	3.05E-08	2.31E-08	34.58
ANB077	1.45E-06	2.36E-08	3.05E-08	2.31E-08	45.97
ANB088	1.58E-06	2.36E-08	3.05E-08	2.31E-08	50.14
ANB092	2.97E-06	2.36E-08	3.05E-08	2.31E-08	95.70
ANB102	6.72E-07	2.36E-08	3.05E-08	2.31E-08	20.50
ANB107	2.75E-07	2.36E-08	3.05E-08	2.31E-08	7.47
ANB118	1.30E-07	2.36E-08	3.05E-08	2.31E-08	2.72
ANB148	3.75E-06	2.36E-08	3.05E-08	2.31E-08	121.28
ANB165	2.00E-06	2.36E-08	3.05E-08	2.31E-08	64.01
ANB233	5.67E-07	2.36E-08	3.05E-08	2.31E-08	17.07
ANB239	1.25E-06	2.36E-08	3.05E-08	2.31E-08	39.37
ANB261	2.00E-07	2.36E-08	3.05E-08	2.31E-08	5.03
ANB262	2.09E-06	2.36E-08	3.05E-08	2.31E-08	66.88
ANB263	9.24E-07	2.36E-08	3.05E-08	2.31E-08	28.78

*All I_d values are presented in ampere (A)

Table S6: The performance correlation in between the Simoa and LM-FET sensor for the quantification of NfL concentration (pg/mL) in serum samples.

Sample ID	Simoa	FET sensor results				
		Mean	SD	CV (%)	Diff. (%)	95% CI
ANB035	37.34	37.74	0.34	0.89	1.067	37.47 - 38.01
ANB053	34.19	34.57	0.91	2.64	1.121	33.84 - 35.30
ANB077	44.8	45.97	1.12	2.44	2.608	45.07 - 46.86
ANB088	49.4	50.14	1.17	2.34	1.495	49.20 - 51.08
ANB092	96.8	95.70	0.48	0.50	-1.135	95.32 - 96.09
ANB102	20.46	20.46	0.07	0.34	0.000	20.40 - 20.52
ANB107	7.26	7.48	0.11	1.52	2.961	7.38 - 7.57
ANB118	2.68	2.72	0.08	2.93	1.555	2.66 - 2.79
ANB148	119.6	121.28	1.88	1.55	1.406	119.78 - 122.79
ANB165	64	17.07	0.21	1.24	-1.472	63.52- 64.50
ANB233	17.32	64.01	0.62	0.96	0.013	16.90 - 17.23
ANB239	39.36	39.37	0.54	1.38	0.025	38.94 -39.80
ANB261	4.98	5.04	0.04	0.76	1.104	5.00 - 5.07
ANB262	65.6	66.89	0.61	0.92	1.959	66.39 - 67.38
ANB263	28.46	28.78	0.33	1.15	1.107	28.51 - 29.04

S5: Sensor production cost analysis

The cost per LM-FET sensor was estimated by dividing the total material or consumable cost used per wafer or batch by the number of sensors produced. In this LM-FET sensor development approach, the sensor layout was designed for fabrication on a 4-inch wafer, with each wafer capable of producing approximately 60 individual sensors. Therefore, wafer-level consumables, such as the 4-inch wafer and positive photoresist (AZ1512 HS), were divided by 60 sensors per wafer. For ultra-thin film material deposition, the MCN e-beam evaporation instrument (Intlvac Nanochrome II) can accommodate up to ten 4-inch wafers in a single chamber run. As each wafer contains approximately 60 sensors, one deposition batch can produce up to 600 sensors. Therefore, the costs of batch-deposited ultra-thin materials, including SiO_2, Pt, and Au, were divided by the estimated batch yield of 600 sensors. The individual material cost contributions were then summed to estimate the total consumable cost per LM-FET sensor. Based on this cost model, the estimated consumable cost was approximately US$0.73 per LM-FET sensor. The cost per sensor was calculated using the following formula, with the detailed calculations presented in Table S7:

$$Cost\ (US\$)\ per\ sensor = \frac{Total\ materials\ or\ consumable\ cost\ of\ per\ wafer\ or\ batch}{Number\ of\ sensor\ produced\ per\ wafer\ or\ batch}$$

Table S7: Estimated consumable cost model for batch fabrication of the LM-FET sensors.

Items	**Unit cost (US$)**	**Usages per wafer/batch**	**Cost per sensor (US$)**
4-inch wafer	$19.50 per wafer	60 sensors	$0.325
Dielectric layer (SiO_2) – 285 nm	$0.040 per nm	600 sensors	$0.0190
Ultra-thin sensing materials (TiO_2) - 30 nm	$0.30 per nm	600 sensors	$0.015
Ultra-thin sensing materials (Pt) – 5 nm	$0.88 per nm	600 sensors	$0.007
Ultra-thin sensing materials (Si) – 5 nm	$0.20 per nm	600 sensors	$0.0016
Electrode material (Au) – 100 nm	$1.62 per nm	600 sensors	$0.270
Photoresist (AZ1512 HS)	$5.40 per wafer	60 sensors	$0.090
Total estimated cost per sensor (US$)			**$0.73**

The fabrication cost of our developed ultra-thin LM- FET sensor is lower (~$0.73) than that of many previously reported nanomaterial-based FET sensors [21], as summarized in Table S8. This cost advantage is mainly attributed to the use of wafer-scale, batch-compatible ultra-thin materials deposition, photolithography, and sensor fabrication processes enabled by MCN capabilities, which allow multiple sensors to be produced simultaneously on a single 4-inch wafer-based substrate. In our sensor design, conductive (Pt), semiconductive (Si), and oxide (TiO_2) materials integrated into an ultra-thin lamellar architecture, reducing material consumption while maintaining high electrical sensitivity, stable gate coupling, and reproducible sensor performance. In contrast, many reported nanomaterial-based FET sensors rely on expensive or low-throughput materials and fabrication steps, such as chemically synthesized graphene, carbon nanotubes, transition-metal dichalcogenides, silicon nanowires or complex transfer/alignment processes, which can increase sensor-to-sensor variability and overall production cost. Therefore, our developed LM-FET sensor demonstrates a cost-effective and scalable route for manufacturing high-performance sensors suitable for future point-of-care diagnostic applications.

Table S8: Benchmarking of the developed LM-FET sensor against previously reported nanomaterials-based FET sensors [21]

Materials	**Sensitivity (LOD)**	**Reproducibility**	**Scalability**	**Cost per sensor (US$)**	**Ref.**
Silicon Nanowires	1 ng/mL	Low	Low	High	[22, 23]
Metal oxide semiconductor	486 ag/mL	Exceptional	Exceptional	Exceptional ~$1.00	[24-26]
Carbon nanotube	0.6 ag/mL	High	High	High ~$2.00	[27-30]
MXene	1 fM	High	moderate	High	[31]
Graphene	0.6 pg/mL	High	High	High ~$15.00	[32]
Transition Metal Dichalcogenides	1 pg/mL	Moderate	Moderate	High	[33-35]
Novel ultra-thin film-based lamellar materials	**7.6 fg/mL**	**Exceptional**	**Exceptional 600 sensors/batch**	**Exceptional ~ 0.73**	**This work**

Supporting information References:

1. Hossain, M.M., et al., *Ultrasensitive WSe2 field-effect transistor-based biosensor for label-free detection of cancer in point-of-care applications.* 2D Materials, 2021. 8(4): p. 045005.
2. Hossain, M.M., et al., *Bisphenol A Detection Using Molybdenum Disulfide (MoS2) Field-Effect Transistor Functionalized with DNA Aptamers.* Advanced Materials Technologies, 2023. 8(11): p. 2201793.
3. Das, S., et al., *High Performance Multilayer MoS2 Transistors with Scandium Contacts.* Nano Letters, 2013. 13(1): p. 100–105.
4. *MOSFETs*, in *Physics of Semiconductor Devices*. 2006. p. 293–373.
5. Banger, K.K., et al., *Low-temperature, high-performance solution-processed metal oxide thin-film transistors formed by a 'sol–gel on chip' process.* Nature Materials, 2011. 10(1): p. 45–50.
6. Fortunato, E., P. Barquinha, and R. Martins, *Oxide semiconductor thin-film transistors: a review of recent advances.* Adv Mater, 2012. 24(22): p. 2945–86.
7. She, J.-W., et al., *Precision Channel Engineering of Nanotube-Embedded Organic Electrochemical Transistors for Ultrasensitive Neurofilament Light Chain Detection.* ACS Applied Bio Materials, 2026. 9(4): p. 2271–2281.
8. Allegrini, F. and A.C. Olivieri, *IUPAC-Consistent Approach to the Limit of Detection in Partial Least-Squares Calibration.* Analytical Chemistry, 2014. 86(15): p. 7858–7866.
9. Kuhle, J., et al., *Blood neurofilament light chain as a biomarker of MS disease activity and treatment response.* Neurology, 2019. 92(10): p. e1007–e1015.
10. Quantrix, *NF-LIGHT®: Ultra-Sensitive NFL Assay for Neurology Research*. 2026.
11. Truffi, M., et al., *Neurofilament-light chain quantification by Simoa and Ella in plasma from patients with dementia: a comparative study.* Scientific Reports, 2023. 13(1): p. 4041.
12. Khetani, S., et al., *μDrop: Multi-analyte portable electrochemical-sensing device for blood-based detection of cleaved tau and neuron filament light in traumatic brain injury patients.* Biosensors and Bioelectronics, 2021. 178: p. 113033.
13. Huang, Z., et al., *Electrochemical Biosensor for Point-of-Care Testing of Low-Abundance Biomarkers of Neurological Diseases.* Analytical Chemistry, 2024. 96(25): p. 10332–10340.
14. Adil, O. and M.H. Shamsi, *Electrochemical Impedance Immunoassay for ALS-Associated Neurofilament Protein: Matrix Effect on the Immunoplatform.* Biosensors, 2023. 13(2): p. 247.
15. Li, W.-t., et al., *A neurofilament-light chains electrochemical immunosensor expected to reveal the early stage of neurodegenerative diseases.* Chemical Engineering Journal, 2022. 446: p. 136850.
16. Kim, K., et al., *Metallic Woodpile Nanostructures for Femtomolar Sensing of Alzheimer's Neurofilament Lights.* ACS Nano, 2020. 14(8): p. 10376–10384.
17. Lin, S.-P., et al., *Nano-Brush Structure for Rapid Label-Free Differentiation of Alzheimer's Disease Stages and Direct Capture of Neuron-Derived Exosomes from Human Blood Plasma.* ACS Applied Materials & Interfaces, 2023. 15(48): p. 56478–56489.
18. Wang, S., et al., *High-Performance Plasma Biomarker Panel for Alzheimer's Disease Screening Using a Femtomolar-Level Label-Free Biosensing System.* ACS Nano, 2024. 18(3): p. 2117–2130.
19. Solodka, K., et al., *Detection of Neurofilament Light Chain with Label-Free Electrolyte-Gated Organic Field-Effect Transistors.* Advanced Materials Interfaces, 2022. 9(11): p. 2102341.
20. Yu, S., et al., *Integrated Microfluidic-Transistor Sensing System for Multiplexed Detection of Traumatic Brain Injury Biomarkers.* ACS Sensors, 2024. 9(6): p. 3017–3026.
21. Deng, F., et al., *Carbon Nanomaterial Field-Effect Transistor Biosensors and DNA-Based Biointerface Engineering.* ACS Nano, 2026. 20(8): p. 6515–6540.
22. Kim, S., et al., *Multiplexed Silicon Nanowire Tunnel FET-Based Biosensors With Optimized Multi-Sensing Currents.* IEEE Sensors Journal, 2021. 21(7): p. 8839–8846.

23. Li, J., et al., *Monitoring of Dynamic Processes during Detection of Cardiac Biomarkers Using Silicon Nanowire Field-Effect Transistors.* Advanced Materials Interfaces, 2020. 7(15): p. 2000508.
24. Yang, Y., et al., *Integrated Urinalysis Devices Based on Interface-Engineered Field-Effect Transistor Biosensors Incorporated With Electronic Circuits.* Advanced Materials, 2022. 34(36): p. 2203224.
25. Li, Y., et al., *Design of high stability thin-film transistor biosensor for the diagnosis of bladder cancer.* Chinese Chemical Letters, 2020. 31(6): p. 1387–1391.
26. Peng, Q., et al., *Interfacial Polymer Engineered Field Effect Transistor Biosensors for Rapid and Efficient Identification of SARS-CoV-2 N Antigen.* Chinese Journal of Chemistry, 2023. 41(18): p. 2253–2260.
27. Liang, Y., et al., *Wafer-Scale Uniform Carbon Nanotube Transistors for Ultrasensitive and Label-Free Detection of Disease Biomarkers.* ACS Nano, 2020. 14(7): p. 8866–8874.
28. Zhu, Z., et al., *Interface Cleaning Strategy of Carbon Nanotube Field-Effect Transistor Biosensors for Ultrasensitive Detection of Ophthalmic Biomarkers.* ACS Applied Materials & Interfaces, 2025. 17(22): p. 33150–33160.
29. Wang, X., et al., *Multifunctional Amyloid-Like Porous Nanofilm-Decorated Transistor-Based Biosensor for Accurate Detection of Alzheimer's Disease Biomarker.* Analytical Chemistry, 2025. 97(31): p. 16832–16840.
30. Hu, X., et al., *Plug-and-play smart transistor bio-chips implementing point-of-care diagnosis of AMI with modified CRISPR/Cas12a system.* Biosensors and Bioelectronics, 2024. 246: p. 115909.
31. Li, Y., et al., *MXene–Graphene Field-Effect Transistor Sensing of Influenza Virus and SARS-CoV-2.* ACS Omega, 2021. 6(10): p. 6643–6653.
32. Bagale, R., et al., *Point-of-Care Applicability of Graphene-Based Field Effect Transistors upon Modification with a Pyrene-Tagged Antifouling Copolymer: Application for cTnI Sensing in Blood.* ACS Sensors, 2025. 10(9): p. 7072–7083.
33. Wei, J., et al., *Highly sensitive detection of multiple proteins from single cells by MoS2-FET biosensors.* Talanta, 2022. 236: p. 122839.
34. Nathiya, D., et al., *Tin disulfide nanoflowers and nitrogen doped graphene oxide based extended gate field effect transistor as immunosensors.* Microchemical Journal, 2024. 199: p. 109904.
35. Wen, X., et al., *Biofunctionalization-optimized MoS2-based FET biosensors for the detection of Tau protein.* Applied Surface Science, 2024. 670: p. 160616.